IOP Publishing Plasma Sources Science and Technology
Plasma Sources Sci. Technol. **27** (2018) 065007 (8pp) https://doi.org/10.1088/1361-6595/aac963

Laser induced fluorescence of Ar-I metastables in the presence of a magnetic field

D S Thompson, T E Steinberger, A M Keesee and E E Scime

West Virginia University, Department of Physics & Astronomy, Morgantown, WV 26506, United States of America

E-mail: dsthompson1@mix.wvu.edu

Received 28 February 2018, revised 3 May 2018
Accepted for publication 1 June 2018
Published 25 June 2018

Abstract

We compare three laser induced fluorescence schemes for measuring velocity distributions of Ar-I $1s_5$ metastables in the presence of a magnetic field. In these three-level schemes, the $1s_5$ state is optically pumped to $2p_2$, $2p_3$, or $2p_4$ by sweeping the frequency of a tuneable CW laser over transitions in the visible range at 696.7352 nm, 706.9167 nm, and 714.9012 nm, respectively. Broadening in the fluorescence spectra is attributed to Zeeman splitting and saturation effects. We present measurements of spectral broadening dependence on injected laser intensity and describe spectral reconstructions that account for Zeeman splitting. For laser injection parallel to a background magnetic field, the separation of the Zeeman-split $\sigma_{\pm}$ clusters is an effective, non-perturbative localized magnetic field diagnostic. We discuss the advantages of the three transition schemes and present the optimal transition for several applications.

Keywords: plasma diagnostics, laser induced fluorescence, neutral velocity distribution functions, Zeeman effect

1. Introduction

Neutral atoms play an important role in determining plasma equilibria and ion dynamics for a wide range of plasma conditions. For example, neutral depletion has been observed in low-temperature plasma sources for some time, and affects plasma density and heating in RF discharges [1–3]. Evidence of ion-neutral Alfvén wave damping has been reported in helicons [4]. The distribution of neutral atoms in Hall thruster channels plays an important part in determining thruster efficiency [5] and, in some models, in setting the conditions for channel erosion [6, 7]. The theory of electrostatic probe characteristics, used to determine electron energy distributions, requires non-perturbative measurements of neutral distributions and flow fields to assess the influence of sheath neutrals in collisional plasmas [8]. In highly-ionized plasmas, neutral atoms at the boundary moderate particle, heat, and momentum loss via charge-exchange collisions with energetic ions [9]. Magnetic confinement devices such as tokamaks and stellarators require neutral particle data in these critical boundary regions to validate sputtering, erosion, and recycling models [7].

Laser induced fluorescence (LIF) has been an effective diagnostic for measuring velocity distribution functions (VDFs) of neutral argon atoms (NVDFs) since the mid-1980s [10–12], following the introduction of Ar-II LIF in 1975 [13]. Since that time, LIF has developed into an established technique for observing the temperature and bulk flow of a wide range of plasma species. As an absorption spectroscopy diagnostic, the high spectral resolution of LIF permits the observation of non-Maxwellian features in velocity distributions in unmagnetized plasmas, and parallel and perpendicular to magnetic field lines [14, 15]. LIF has been used to interrogate pulsed plasmas [16], measure multiple spatial dimensions simultaneously [17–20], record distributions changing in time [21], and isolate the effects of instabilities [22].

Optimal LIF techniques take advantage of absorption transitions in the visible range, where specialized optics and sensors are not required, and observe long-lived, metastable states that closely approximate the ground state. In argon, such metastable techniques have been used to study reaction

kinetics using pulsed lasers [23], to achieve high velocity-resolution using Lamb dip spectroscopy [24], and to measure state distributions in unmagnetized plasmas [23, 25].

In this work, we report three-level, single-photon LIF measurements of NVDFs from the metastable $1s_5$ state of argon in a magnetized plasma. While LIF measurements using this state have been reported previously, few investigations have observed these transitions in the presence of a magnetic field [26]. We describe spectral broadening effects for measurements along and perpendicular to the magnetic field. We demonstrate a method that uses the Zeeman splitting of LIF spectra as a non-perturbative, localized magnetic field diagnostic. Three transition schemes in the pump wavelength range 696–715 nm are compared. Each of the three schemes has its advantages and disadvantages, and we identify the optimal application for each one.

2. Experimental configuration

2.1. LIF of Ar-I metastables

The ground state of a neutral argon atom exists in the $1s^2 2s^2 2p^6 3s^2 3p^6$ electron configuration. The lowest energy group of Ar-I excited states occurs when one of the outer electrons occupies the $3p^5 4s$ levels, and in Paschen's notation these states are referred to as $1s_5$, $1s_4$, $1s_3$, and $1s_2$ in order of increasing energy. Successful techniques for measuring NVDFs from the resonant $1s_2$ and $1s_4$ states are accessible using relatively inexpensive diode lasers [27–30]. LIF measurements originating from these states have limited applicable pressure ranges because $1s_2$ and $1s_4$ are primarily populated through electron-impact collisions with atoms in metastable states $1s_3$ and $1s_5$, respectively, and are only weakly populated from the ground state. In one helicon plasma, $1s_4$ measurements were limited to neutral pressures greater than 6.0 mTorr [29].

LIF spectra represent the ground state when the lifetime of the interrogated state is long enough that the population has time to thermalize. Therefore, LIF is only able to provide information on effects whose interaction lifetime is much smaller than the state lifetime. A disadvantage of the $1s_2$ and $1s_4$ states is that their lifetimes are on the order of 10 ns, and extrapolation from these states to the ground state is valid for a limited set of very fast interactions. (For a discussion on related lifetime effects in argon ions, see [31–33].)

Of the two metastable states, the $1s_3$ state is expected to be only sparsely populated in low-temperature plasmas, whereas the $1s_5$ state number density has been found to approximate the neutral ground state [25]. In the same experiment, the ratio of the $1s_5$-to-$1s_3$ number densities was found to approximate the statistical weights of the two states, such that the signal-to-noise ratio (SNR) of $1s_5$ data is expected to be a factor of 5 higher than the SNR using $1s_3$.

In the experiments reported here, we interrogate the lowest excited-energy metastable state, $1s_5$, which has a reported lifetime up to tens of seconds [34]. The $1s_5$ state is optically pumped to upper state $2p_2$ at (vacuum) rest wavelength 696.7352 nm, to $2p_3$ at 706.9167 nm, and to $2p_4$ at 714.9012 nm. The energies and transitions used in the measurements reported here are shown in figure 1. The spectroscopic details of the three $1s_5$ schemes, as well as the details of the $1s_4$ scheme used for comparison, are described in table 1.

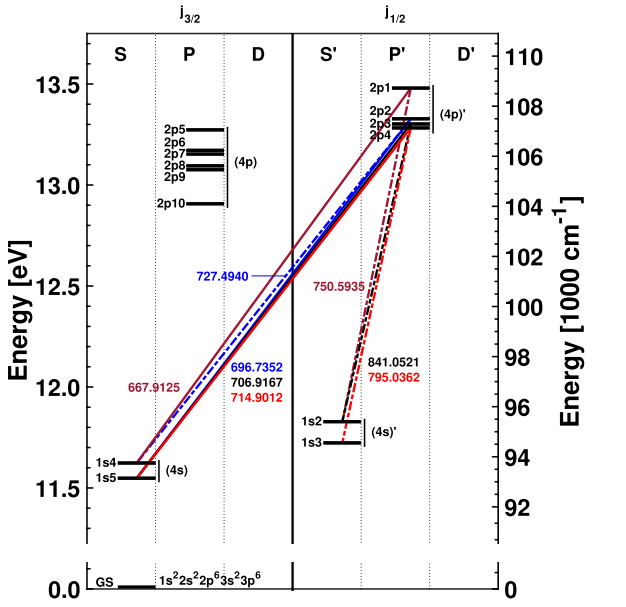

Figure 1. Energy level diagram for Ar-I showing energy levels and transitions for schemes 1–4.

Distribution moments are obtained from LIF data by fitting a single-Maxwellian function to the intensity spectrum:

$$I(\nu) = \alpha + \beta \exp\left[-\gamma(\nu - \nu_o - (\bar{U}_n/c)\nu_o)^2\right]. \quad (1)$$

In (1), I is the fluorescence intensity collected as the laser is swept over ν, the frequency of the injected laser. ν_o is the transition frequency of the absorbing population at rest, c is the speed of light, and $(\bar{U}_n/c)\nu_o$ is the spectral Doppler shift due to mean absorber flow. The fit parameters α, β, and $\bar{U}_n$ give the DC background, normalization constant, and mean flow of the absorbing species distribution, respectively. $\gamma = m_n c^2/2k_B T_n \nu_o^2$ scales the distribution width according to the ratio of the kinetic and thermal energies, where m_n is the mass of the argon atom, k_B is the Boltzmann constant, and T_n is the temperature of the interrogated population.

Linewidth effects must remain small compared to Doppler broadening for (1) to be valid. The laser linewidth is $<$20 MHz in schemes 1–3 (which use a tuneable CW dye laser) and is $<$1 MHz in scheme 4 (which uses a tuneable CW diode laser). Stark effect broadening has been calculated to be $\lesssim$50 MHz for similar plasma conditions [35] and is negligible compared to the Doppler broadening. The natural linewidth, $\Delta\nu$, of the absorption transitions is approximately 5.5 MHz for the metastable transitions in schemes 1–3 and is 26.1 MHz for scheme 4. These natural linewidths, calculated using transition probabilities from Wiese *et al* [36], are shown in table 2. All of these linewidths are much smaller than the Doppler width, which at room temperature is $>$1 GHz, and are appropriately neglected in (1). The larger of the natural

Table 1. Summary of Ar-I laser induced fluorescence schemes examined in these measurements. The Ar-I ground state is $1s^2\,2s^2\,2p^6\,3s^2\,3p^6$. λ_{12} indicates the absorption wavelength and λ_{23} indicates the fluorescence wavelength. Vacuum wavelengths are given in all cases. A_{21} and A_{23} are the spontaneous emission coefficients associated with each transition.

Transition scheme	Transition scheme (Paschen)	Transition scheme (Racah)	λ_{12} (nm)	λ_{23} (nm)	A_{21} (s^{-1})	A_{23} (s^{-1})
1	$1s_5 \rightarrow 2p_2 \rightarrow 1s_4$	$4s(^2P^o_{3/2})_2$–$4p'(^2P^o_{1/2})_1$–$4s(^2P^o_{3/2})_1$	696.7352	727.4940	6.39×10^6	1.83×10^6
2	$1s_5 \rightarrow 2p_3 \rightarrow 1s_2$	$4s(^2P^o_{3/2})_2$–$4p'(^2P^o_{3/2})_2$–$4s'(^2P^o_{3/2})_1$	706.9167	841.0521	3.80×10^6	2.23×10^7
3	$1s_5 \rightarrow 2p_4 \rightarrow 1s_3$	$4s(^2P^o_{3/2})_2$–$4p'(^2P^o_{3/2})_1$–$4s'(^2P^o_{1/2})_0$	714.9012	795.0362	6.25×10^5	1.86×10^7
4	$1s_4 \rightarrow 2p_1 \rightarrow 1s_2$	$4s(^2P^o_{3/2})_1$–$4p'(^2P^o_{1/2})_0$–$4s'(^2P^o_{1/2})_1$	667.9125	750.5935	2.36×10^5	4.45×10^7

Table 2. Quantities related to various broadening mechanisms are shown for each of the four schemes. $\Delta\nu$ is the natural linewidth of the absorption transition. ϵ_Z indicates the Zeeman shift for a 1 mT magnetic field; both calculated and observed values are given. $\Delta\,\nu_{Z\pi}$ and $\Delta\,\nu_{Z\sigma}$ are the Zeeman broadening (FWHM) of the π and σ lines, respectively, for a 1 mT magnetic field.

Transition Scheme	λ_{12} (nm)	$\Delta\nu$ (MHz)	ϵ_Z calc. (MHz mT^{-1})	ϵ_Z obs. (MHz mT^{-1})	$\Delta\nu_{Z\pi}$ (MHz mT^{-1})	$\Delta\nu_{Z\sigma}$ (MHz mT^{-1})
1	696.7352	5.6	21.8	21.4 ± 0.3	4	5
2	706.9167	5.5	20.6	19.0 ± 0.1	21	12
3	714.9012	5.3	25.8	22.8 ± 0.3	25	30
4	667.9125	26.1	14.0 [28]	(Not measured)	0	0

and laser linewidths sets the spectral resolution for the transition scheme. For the metastable transitions of schemes 1–3, the narrow natural linewidth sets an ideal flow measurement uncertainty of 4 m s^{-1}. For the dye laser measurements reported here, the natural linewidth is dominated by the linewidth of the dye laser, which at 20 MHz corresponds to a minimum velocity uncertainty of 14 m s^{-1}. The relatively large natural linewidth of the scheme 4 absorption transition, at 26.06 MHz, is a result of the large transition probability from the $1s_4$ state to the ground state and results in a minimum velocity uncertainty of 17 m s^{-1}. In practice, the shot-to-shot variation is several 10s of m s^{-1} and sets the overall uncertainty when measuring neutral flow.

An external magnetic field splits the spectrum into π ($\Delta\, m = 0$) and $\sigma_\pm$ ($\Delta\, m = \pm\, 1$) components due to the Zeeman effect. The resulting spectrum is described by the sum of k constituent distributions, each with relative intensity β_i and offset $\delta\nu_i$ determined from atomic calculations [37]:

$$I(\nu) = \alpha + \sum_{i=1}^{k} \beta_i \exp\left[-\gamma(\nu - \nu_o - (\bar{U}_n/c)\nu_o - \delta\nu_i)^2\right]. \tag{2}$$

In (2), γ is assumed to be common across all components and provides an accurate measure of T_n when Doppler broadening dominates.

For LIF measurements perpendicular to the magnetic field, the $\sigma_\pm$ groups are filtered out by placing a linear polarizer in the laser beam path, and only the π lines contribute to the recorded spectrum. In many cases, the internal Zeeman splitting of the π lines is negligible compared to the Doppler broadening of the distribution and the simpler (1) provides an accurate measure of T_n. In weak magnetic fields, the Zeeman effect manifests as a broadened spectrum, but the individual components are not resolved. In these cases, we refer to initial analyses that neglect Zeeman splitting and apply (1) as 'naive'. In the full treatment, the internal Zeeman splitting is included and (2) is used to obtain T_n.

For LIF measurements parallel to the field, the spectrum contains only the $\sigma_\pm$ clusters. If the laser beam is unpolarized, $\bar{U}_n$ and T_n are calculated by fitting a pair of curves which have the functional form of (2). The frequency offset of the $\sigma_\pm$ cluster peak intensities is denoted ν'_Z and is proportional to the magnetic field magnitude. In weak magnetic fields where the two clusters cannot be resolved, circular polarization of the laser with a quarter-wave plate isolates one of the groups. T_n is then determined using (1), and $\bar{U}_n$ is determined when ν'_Z is known in advance.

Two additional effects—laser power and pressure broadening—must be considered. Laser power broadening [38, 39], alternatively referred to as saturation broadening, occurs when the fluorescence intensity saturates from absorption depopulation of the initial state. When this happens, the measured emission does not vary significantly with laser frequency within a finite region around peak absorption, producing a spectrum that is artificially broad. Pressure broadening occurs as a result of the Stark effect from the electric fields of charged particles during collisions with the probed neutral species. Broadening due to increased collisionality manifests as an increase in the spectral width with increasing pressure. This effect is predicted to be small relative to Doppler broadening at pressures $\lesssim$100 mTorr [37].

2.2. The HELIX facility

The spectra reported here were measured in the HELIX plasma source. The HELIX facility [40] is capable of generating radio-frequency plasmas in capacitive, inductive, and

helicon operation modes, permitting ion and neutral VDF measurements in plasma conditions from $n = 10^{15}$–10^{19} m^{-3}, $B \lesssim 120$ mT, $T_e = 2$–10 eV, and $T_i = 0.1$–0.5 eV. Two turbomolecular pumps, each capable of pumping at 1600 l s^{-1}, maintain a base vacuum of 10^{-7} Torr in the chamber. Argon gas is introduced through an MKS mass flow controller at the end of the chamber opposite to the pumps. Ten electromagnets maintain a uniform field ($\delta B/B < 1\%$) throughout HELIX which is confirmed by a calibrated Hall effect gaussmeter. Optical access is provided by 6 inch windows, the center of which is located 69 cm downstream of a copper strap half-turn $m = +1$ helicon antenna.

The dye laser optical arrangement used for the metastable $1s_5$ measurements (schemes 1–3) is described and diagrammed in a recent publication [41]. In this arrangement, a Sirah Matisse dye ring laser produces up to approximately 350 mW of laser power by pumping Pyridine 1 dye dissolved in ethylene glycol. The wavelength of the output is selected by adjusting bi-refringent and piezo-electric controlled etalon components within the laser cavity. The stable wavelength range of the laser is 689–742 nm, with maximum output at approximately 712 nm. Immediately upon exiting the laser cavity, the beam splits and approximately 1 mW is directed into a Bristol 621 wavemeter which records the input power and wavelength, with $\delta P_{\rm las}^{\rm w.m.}/P_{\rm las}^{\rm w.m.} = \pm 15\%$ and $\delta\lambda_{\rm las} = \pm 0.0001$ nm. For injection across **B**, the laser is transmitted to the HELIX chamber in an adjacent room via a 200 μm core multimode optical fiber, where it is recollimated into a $\varnothing 3.9 \pm 0.1$ mm ($1/e^2$-level) Gaussian beam before entering the plasma column. For injection along **B**, a 10 μm core fiber is used, and the laser is collimated into a $\varnothing 2.1 \pm 0.1$ mm Gaussian beam. For total laser power in mW, and beam diameter $d = 4\sigma$ in millimeters, the peak laser intensity is $I_{{\rm las},o}(10^{-3}\,{\rm W\,m^{-2}}) = 8P_{\rm las}/\pi d^2$. Coupling into the narrower fiber reduces the transmitted power by a factor of approximately four, however the beam size decreases by the same amount, so the intensity is comparable between the two directions. The final power injected into the plasma is controlled by passing the laser through a pair of offset linear polarizers in rotational mounts. Fluorescent emission from the plasma is collected through an $f/\# = 4$ lens and focused into a $\varnothing 1$ mm core multimode optical fiber. Previous implementations of this dye laser arrangement have isolated the fluorescence wavelength with narrow bandpass filters. In the implementation used for this report, such filters were unavailable at the desired wavelengths. Instead, the collected light passes through a McPherson Model 209 1.33 m Czerny–Turner scanning monochrometer, which serves as a ± 5 nm filter. The passband of the monochrometer is confirmed by recording the spectrum of an Ar standard lamp with an SBIG STF-8300M CCD. LIF signal is recorded by a Hamamatsu HC120-05MOD IR-sensitive photomultiplier tube (PMT) placed at the primary outlet of the monochrometer. To isolate the fluorescence signal from electron-impact emission and electronic noise, the PMT output undergoes lock-in amplification referenced to a 5 kHz mechanical chopper in the injection beam path. For the non-metastable $1s_4$ measurements (scheme 4), a Toptica DL 100 master oscillator power amplifier laser replaces the dye laser in the optical arrangement. Wavelength isolation of the fluorescence is achieved by a 1 nm bandpass filter in the collection path. A stationary molecular iodine gas cell is used as a frequency reference for the diode laser [28]. Except for the laser, wavelength filter and iodine cell, all other components are identical for all four schemes.

No viable iodine lines are observed in the near vicinity of any of the wavelengths used in schemes 1–3. Instead, the laser frequency is calibrated using a fixed volume argon Opthos Instruments Inc. cell inserted into an Evenson 2.45 GHz microwave resonant cavity [42, 43]. The gas in the closed cell is assumed to have zero mean flow. Each LIF transition is calibrated by recording a pair of NVDFs in which the laser passes through the cell along counter-propagating paths, parallel and antiparallel to the cell axis. We observe no displacement between the counter-propagating NVDFs, which validates the zero mean flow assumption in the cell. The zero velocity location of these spectra provides the reference for subsequent measurements.

3. Results and discussion

3.1. Ar-I LIF $\perp$ B

Ar-I NVDFs were recorded on-axis in an inductive plasma generated in 2–16 mTorr argon gas with 400 W of RF power. The laser was injected perpendicular to the 45 mT magnetic field. In HELIX, plasmas created under these conditions typically exhibit $T_e \approx 3$ eV, $T_i \approx 0.3$ eV, and $n \approx 10^{17}$–10^{18} m^{-3}. Each full spectrum was captured with a 5 GHz sweep centered at the absorption resonance. Sufficient SNR was obtained by passing the lock-in amplifier output through a 3 s time constant filter. The ratio between the sweep time and the time constant is an important quantity. A longer time constant improves noise suppression, but increasing the time constant to a large fraction of the total sweep applies a strong low-pass filter to the spectrum, flattening the spectrum and shifting the peak toward frequencies later in the sweep. For $1s_5$ spectra, a single 540 s sweep and 3 s time constant preserved spectral shape in preliminary measurements. The diode laser for scheme 4 consisted of 20 s sweeps and a 100 ms time constant, with twenty-seven sweeps averaged for each spectrum.

$1s_5$ spectra were recorded for a range of fill pressures at consistent magnetic field, forward RF power, and injected laser intensity. The dependence of the spectral FWHM on fill pressure is shown in figure 2. The absence of a monotonic trend with fill pressure in these data is consistent with ignorable pressure broadening. Only scheme 3 shows any increase with greater pressure, with the FWHM expanding only 4 MHz mTorr^{-1}. At the same time, the uncertainty in the fit to (1) for these data is 44 MHz (0.002 eV), with shot-to-shot variation exceeding 100 MHz at some pressures. Therefore, we do not measure any significant pressure broadening in this pressure range. There is a significant disparity between the three schemes, however: schemes 2 and 3 produce mean FWHM that are 11% and 30% larger than the

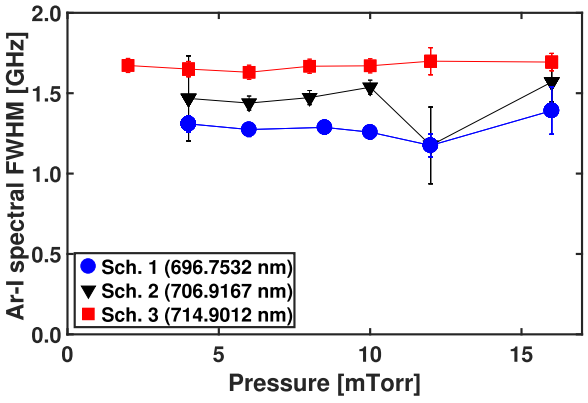

Figure 2. Spectrum FWHM dependence on fill pressure for schemes 1–3 at $B = 45$ mT and $P_{rf} = 400$ W. Pressure uncertainty is approximately 0.1 mTorr. FWHM uncertainty is calculated from the quadrature sum of the confidence interval of the fit quantities and the shot-to-shot variation at each pressure.

FWHM of scheme 1, and naive single-Maxwellian fits to these spectra produce mean temperatures 0.030, 0.039, and 0.053 eV for schemes 1–3, respectively. The underlying cause of this disparity is a combination of the laser power and Zeeman broadening effects.

As shown by Goeckner *et al* [38], the threshold for saturation broadening during LIF measurements in a plasma is not accurately predicted by the classic ratio of the pumping rate to the spontaneous emission rate out of the absorbing state. In some cases they observed a factor of 10^2 difference in saturation threshold intensity between experiment and predictions from sophisticated atomic modeling. Additions to the absorbing state population from direct excitation from the ground state and losses due to collisions introduce significant corrections to the saturation threshold. The shape of the laser beam profile may also change the saturation threshold by one to two orders of magnitude [38]. For each of the four schemes used here, the predicted saturation thresholds range from 1.6×10^3 to 1.5×10^4 W m^{-2} [44]. Depending on the profile of the 3.9 mm diameter Gaussian beam, the peak laser intensities used here range from approximately 3×10^2 to 1.65×10^4 W m^2. To determine the actual impact of laser power broadening on the spectral width of the three $1s_5$ schemes, spectra were recorded while varying the laser intensity injected into a plasma generated in 6 mTorr argon gas with 400 W RF power in a 45 mT magnetic field. Earlier experiments indicated that the saturation threshold for scheme 4 was approximately 2.5×10^3 W m^{-2} in higher neutral pressure (more collisional) plasmas. The spectral widths of these data are depicted as solid icons in figure 3. The laser power uncertainty, set by the power meter, is ±2 mW, so $\delta I_{las} = 300$ W m^{-2}. Scheme 1 shows the greatest sensitivity to laser power broadening, with the FWHM increasing from 1.22 GHz (0.027 eV if a single-Maxwellian distribution is assumed) at 5.10×10^2 W m^{-2} injected power to 1.49 GHz (0.040 eV) at 1.27×10^4 W m^{-2}, a 22% increase. Similarly, the scheme 2 FWHM increased from 1.44 GHz at 5.10×10^2 W m^{-2} to 1.68 GHz at 1.23×10^4 W m^{-2}, a 17% increase. In contrast, the scheme 3 FWHM increased by only 10% over the same range. The non-metastable FWHM measured by scheme 4 is 1.17 ± 0.10 GHz (0.025 ± 0.004 eV). Only scheme 1 produces a FWHM within uncertainty of the $1s_4$ data at low powers. At these powers, scheme 2 tends toward the $1s_4$ width, but still exceeds it by 0.27 GHz at $I_{las,o} = 5.10 \times 10^3$ W m^{-2}. The FWHM measured by scheme 3 is nearly flat over this power range and does not appear to tend toward the $1s_4$ level at any power. The shot-to-shot variation in these data is small, and in combination with the fit confidence, the FWHM uncertainty is estimated to be 0.049 GHz for the three metastable schemes. In summary, power broadening sufficiently accounts for the laser intensity dependence of the FWHM measured by scheme 1, but is insufficient to explain the behavior of the other two metastable schemes.

Internal Zeeman splitting of the π lines accounts for the remaining difference between the FWHM obtained by schemes 2 and 3, and the width observed in the $1s_4$ measurements that is corroborated by the scheme 1 width at low laser intensity. As described in section 2.1, Zeeman broadening can be estimated by reconstructing LIF data using atomic transition models. The frequency offset of the individual components is calculated for a given magnetic field strength using the Landé g-factors for the initial and final states of the absorption transition. For states that follow Russel–Saunders (LS) coupling, the Landé g-factors are calculated from the angular momentum S, orbital angular momentum L, and total angular momentum J. However, the states of the argon atom (and other rare gases) are dominated by jj-coupling or some intermediate coupling, and it is best to use observed g-factors from literature [45]. For a 1 mT magnetic field, the FWHM in frequency space of the π lines, $\Delta \nu_{Z\pi}$, and of the σ lines (for each of the two clusters separately), $\Delta \nu_{Z\sigma}$, are shown in table 2. Scheme 3 has the largest Zeeman broadening and scheme 1 has the smallest, consistent with the trend observed in the FWHM variation. Scheme 4 has no Zeeman broadening because the transition only has one π line and two symmetric σ lines.

In reconstructing LIF spectra, the spectrum is described by (2), which sums over the π components. Example spectra reconstructed in this way are shown in figure 4. A nonlinear least-squares fitting algorithm determines the magnitude and shared temperature of these distributions. The temperatures that emerge reflect any power broadening present but exclude Zeeman effects. The corresponding FWHM are referred to as 'Zeeman corrected' in figure 3 and are denoted by hollow icons. The spectral widths determined by the atomic models are not significantly different from the widths of the data for scheme 1, as is expected for the modest offset of the π components in that scheme. In contrast, the widely set π components of the scheme 3 transition result in a dramatic reduction in the FWHM, reducing the mean FWHM from 1.62 to 1.18 GHz. This latter reconstructed width corresponds to a temperature of 0.027 eV, whereas naive fits to the data suggest a mean temperature of 0.045 eV. When combined with power broadening mitigation, atomic transition reconstructions bring the $1s_5$ temperature derived from scheme 3 to within several thousandths of an eV of a gas in thermal

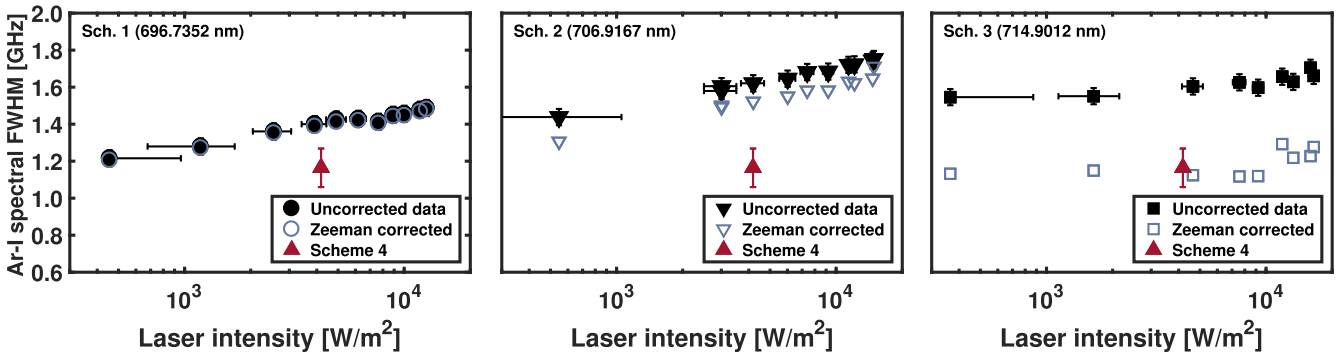

Figure 3. FWHM dependence on peak instantaneous injected laser intensity for (metastable) schemes 1–3 at $B = 45$ mT, $P_{rf} = 400$ W, and $p = 6$ mTorr. The FWHM measured by (non-metastable) scheme 4 corresponds to a neutral temperature of 0.025 ± 0.004 eV recorded at $I_{las,o} = 4.22 \times 10^3$ W m^{-2}. The solid shapes indicate single-Maxwellian fits to the original spectra. The hollow shapes indicate the distribution FWHM determined after Zeeman broadening effects have been removed by atomic model reconstructions. FWHM uncertainty for these data, from shot-to-shot variation and fit uncertainty, is ±49 MHz.

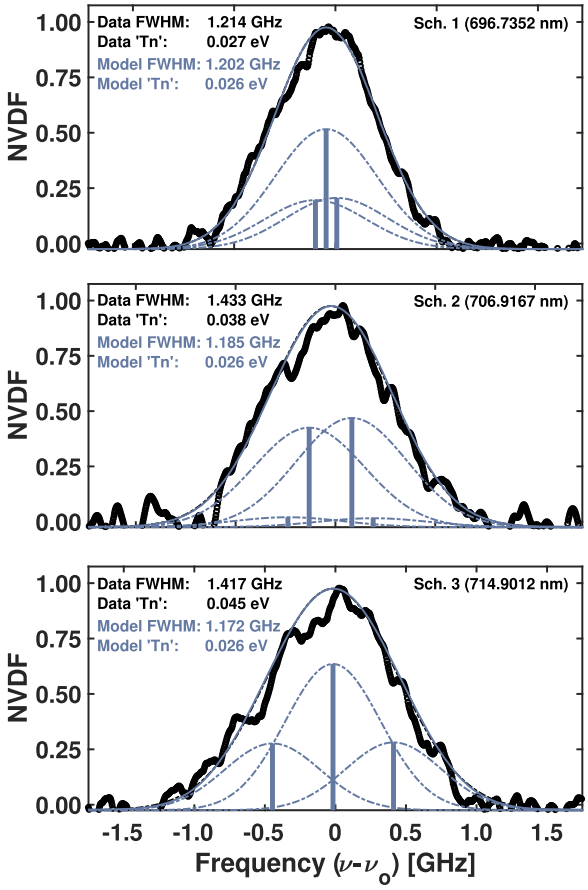

Figure 4. Spectral reconstructions of spectra from schemes 1–3 showing Zeeman-split π components and constituent distributions. Fits to the data are shown as black dashed curves. Constituent distributions are shown as blue dotted–dashed curves. The sum of the constituent distributions is shown in solid blue.

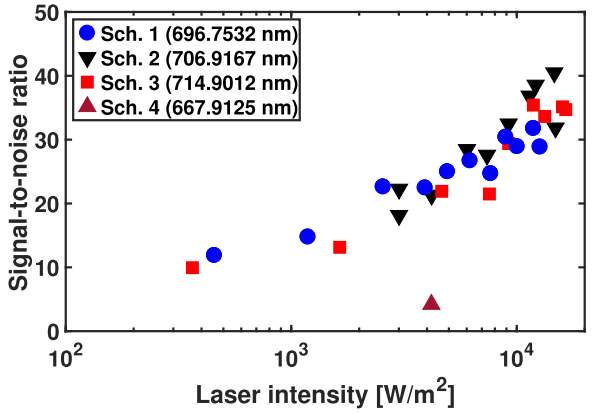

Figure 5. SNR dependence on peak instantaneous injected laser intensity at $B = 45$ mT, $p = 6$ mTorr and $P_{rf} = 400$ W.

equilibrium with the chamber walls and of T_n derived from the $1s_4$ data.

At each laser intensity the three metastable schemes have comparable SNR, as shown in figure 5. These schemes demonstrate a clear improvement in SNR over the non-metastable scheme, which at 4.22×10^3 W m^{-2} exhibits a factor of 2 lower SNR than the metastable data recorded with 5.10×10^2 W m^{-2}. This increased SNR from probing $1s_5$ extends Ar-I LIF to plasmas for which the $1s_4$ signal is inadequate.

3.2. Ar-I LIF ∥ B

A typical Zeeman-split spectrum, observed for laser injection parallel to the magnetic field direction, is shown in figure 6. At these temperatures, an 8 GHz sweep captures the full spectrum. The unpolarized laser beam excites both σ groups, and a $2\nu'_Z$ separation of the two peaks occurs with the center of the total distribution occurring at $\nu = \nu_o(1 + \bar{U}_n/c)$. The theoretical separation can be predicted from the average shift of each Zeeman σ cluster based on the offsets and intensities of its components [46].

The magnetic field dependence of the $\sigma_\pm$ separation is shown in figure 7 for schemes 1–3. The dependence is linear for magnetic fields in the range 20–100 mT, such that the Zeeman shift can be written $\nu'_Z = \epsilon_Z B$, with ϵ_Z for each scheme determined from the slope of the linear trend. The observed values of ϵ_Z are shown in table 2 and coarsely agree with predicted values. The difference between prediction and observation likely arises from attributing a Gaussian shape to a distribution that is actually slightly non-Gaussian, in which

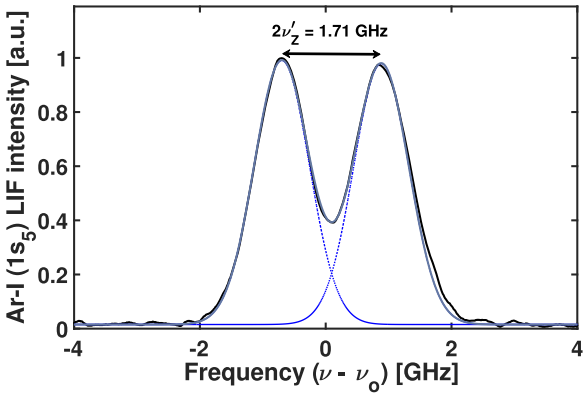

Figure 6. Zeeman-split $\sigma_\pm$ groups observed using scheme 1 at $B = 40$ mT, $p = 6$ mTorr, and $P_{rf} = 400$ W. The spectrum center frequency marks the mean flow of the absorbing $1s_5$ population. The frequency separation of the two peaks is therefore twice the Zeeman shift.

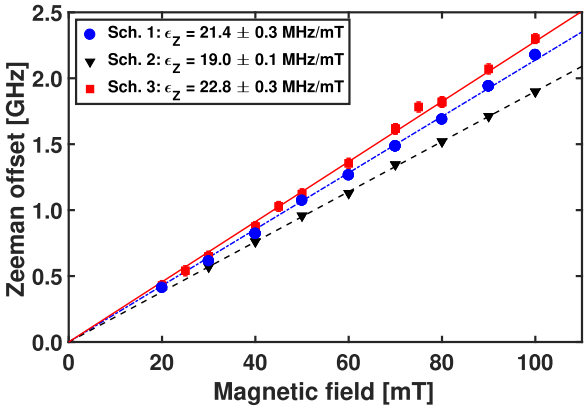

Figure 7. Measured Zeeman shift dependence on magnetic field, comparing schemes 1–3 at $p = 6$ mTorr and $P_{rf} = 400$ W. $\delta\nu'_Z \lesssim 0.04$ GHz for all three schemes, and $\delta B < 1$ mT.

the peak—used in observation—and the mean—used for prediction—are slightly offset. Regardless, the measurement uncertainty $\delta\nu'_Z$ is dominated by shot-to-shot variation and is estimated to be 26 MHz, 10 MHz, and 38 MHz, for schemes 1–3, respectively. When calculating $\bar{U}_n$, a conservative estimate of $\delta\nu'_Z \approx 40$ MHz provides an upper bound of 29 m s^{-1} to the uncertainty in mean flow. The quadrature sum of the uncertainties in the fits of the two peaks contributes an additional ±5 MHz for all schemes. The $\sigma_\pm$ peak separation provides a magnetic field diagnostic, localized to the intersection region of the laser beam and collection sightlines, for which the uncertainty in the field magnitude is given by

$$\delta B/B = [(\delta\nu'_Z/\nu'_Z)^2 + (\delta\epsilon_Z/\epsilon_Z)^2]^{1/2}. \quad (3)$$

In the measurements reported here, $(\delta\epsilon_Z/\epsilon_Z)^2 \sim 10^{-4}$ and in the worst case, where small magnetic fields produce small cluster separation, $(\delta\nu'_Z/\nu'_Z)^2 \sim 10^{-2}$. At a representative low field of 20 mT, where the clusters are close and difficult to resolve, a conservative estimate of the magnetic field uncertainty (with cluster separation uncertainty kept below 40 MHz) is $\delta B/B \approx 10\%$. This figure drops below 5% above 40 mT and decreases with increasing field strength. In these low fields, the differences between the the observed and calculated ϵ_Z in table 2 contribute <1% to $\delta B/B$. The first term of (3) dominates until approximately 100 mT, at which point it becomes small compared to the uncertainty in ϵ_Z and the total uncertainty asymptotes to slightly more than 1%.

4. Summary

We have presented three LIF schemes which exploit visible wavelength pump transitions from the metastable $1s_5$ state to measure the Ar-I VDFs in the presence of a magnetic field. All three metastable schemes provided a factor of ≈4 higher SNR than the $1s_4$ scheme at similar laser intensity. The three $1s_5$ schemes differ in their susceptibility to laser saturation and Zeeman broadening. The transitions to $2p_2$ at 696.7352 nm (scheme 1) and $2p_3$ at 706.9167 nm (scheme 2) exhibit the greatest sensitivity to laser power broadening. The spectral widths from these measurements compare well with the established non-metastable $1s_4$ scheme at 667.9125 nm (scheme 4). Due to its negligible Zeeman broadening and superior SNR compared to non-metastable methods, the $2p_2$ transition of scheme 1 is the optimal scheme for measuring detailed velocity distributions perpendicular to the magnetic field if saturation broadening is avoidable. Where Zeeman broadening is present, as in schemes 2 and 3, it is not possible to spectrally resolve non-Maxwellian distribution features, however it is often feasible to avoid distortion from saturation. Scheme 1 has the additional benefit of having the shortest fluorescence wavelength, making it best suited for detectors with reduced sensitivity in the infrared range. The influence of laser saturation changes with plasma conditions and laser optics, and we recommend carefully selecting the laser power before using any of the LIF schemes described here. A simple approach is to decrease the laser power until reducing the laser power further produces no change in FWHM. *Goeckner et al* have proposed several additional methods [38].

The transition to $2p_4$ at 714.9012 nm (scheme 3) is the least susceptible to laser saturation. However, this scheme exhibits significant internal Zeeman broadening that requires careful atomic modeling to obtain accurate temperatures. This scheme is therefore ideal for low signal conditions, where additional laser power is needed to increase the SNR without introducing temperature error. This scheme is disadvantageous for discerning non-Maxwellian distribution features, which cannot be extracted from the data unless the magnetic field is very weak or sufficiently strong to separate the individual lines entirely. Parallel spectra measured at magnetic fields $\gtrsim$20 mT were sufficient to resolve the two Zeeman-split $\sigma_\pm$ clusters. We have shown that the separation of these clusters depends linearly on the magnetic field. The linear coefficient that scales the σ cluster separation from the magnetic field amplitude was found to be approximately 20 MHz mT^{-1} for all three transitions. The measured coefficients coarsely agree with predictions from atomic models that incorporate Landé g-factors from observation. The models match the qualitative relationship between the three

transitions, but consistently overestimate the separation observed by several percent. The separation of the Zeeman-split σ clusters was used to directly measure the magnitude of the background magnetic field. Due to the uncertainty of this coefficient and to uncertainties within LIF measurements, we found that obtaining magnetic field measurements with uncertainties below 10% were feasible in these plasma conditions and that low single-digit percent uncertainties are possible in higher fields. All three metastable schemes are appropriate for measuring the magnetic field, however the $2p_3$ transition (scheme 2), at $\pm 0.1\,\mathrm{MHz\,mT^{-1}}$ offers slightly better precision than the other two schemes. This scheme is the least suitable for magnetic fields $\lesssim$30 mT due to the difficulty of resolving the separate peaks as a result of its narrower Zeeman separation. Schemes 1 and 3 are better suited to measure these low fields.

Acknowledgments

This work is supported by U.S. National Science Foundation Grant Nos. PHY-1360278 and PHY-0918526. The authors thank Takeru Furukawa for contributing preliminary measurements, and N Ivan Arnold and Stuart Loch for helpful atomic modeling discussions.

ORCID iDs

D S Thompson https://orcid.org/0000-0003-0773-3023

References

[1] Gilland J, Breun R and Hershkowitz N 1998 *Plasma Sources Sci. Technol.* **7** 416
[2] Denning C M, Wiebold M and Scharer J E 2008 *Phys. Plasmas* **15** 072115
[3] Fruchtman A 2017 *J. Phys. D: Appl. Phys.* **50** 473002
[4] Watts C and Hanna J 2004 *Phys. Plasmas* **11** 1358
[5] Fruchtman A, Fisch N J and Raitses Y 2001 *Phys. Plasmas* **8** 1048
[6] Cho S, Komurasaki K and Arakawa Y 2013 *Phys. Plasmas* **20** 063501
[7] Siddiqui M U, Thompson D S, Jackson C D, Kim J F, Hershkowitz N and Scime E E 2016 *Phys. Plasmas* **23** 057101
[8] Demidov V I, Ratynskaia S V and Rypdal K 2002 *Rev. Sci. Instrum.* **73** 3409
[9] Magee R M, Galante M E, McCarren D, Scime E E, Boivin R L, Brooks N H, Groebner R J, Hill D N and Porter G D 2012 *Rev. Sci. Instrum.* **83** 10D701
[10] Ferreira C M, Loureiro J and Ricard A 1985 *J. Appl. Phys.* **57** 82
[11] McMillin B K and Zachariah M R 1995 *J. Appl. Phys.* **77** 5538
[12] Hebner G A 1996 *J. Appl. Phys.* **80** 2624
[13] Stern R A and Johnson J A III 1975 *Phys. Rev. Lett.* **34** 1548
[14] Aguirre E M, Scime E E, Thompson D S and Good T N 2017 *Phys. Plasmas* **24** 123510
[15] Sadeghi N, Nakano T, Trevor D J and Gottscho R A 1991 *J. Appl. Phys.* **70** 2552
[16] Scime E E, Biloiu C, Compton C, Doss F, Venture D, Heard J, Choueiri E and Spektor R 2005 *Rev. Sci. Instrum.* **76** 026107
[17] Bogaerts A, Guenard R D, Smith B W, Winefordner J D, Harrison W W and Gijbels R 1997 *Spectrochim. Acta* B **52** 219
[18] McMillin B K and Zachariah M R 1996 *J. Appl. Phys.* **79** 77
[19] Hansen A K, Galante M, McCarren D, Sears S and Scime E E 2010 *Rev. Sci. Instrum.* **81** 10D701
[20] Hood R, Scheiner B, Baalrud S D, Hopkins M M, Barnat E V, Yee B T, Merlino R L and Skiff F 2016 *Phys. Plasmas* **23** 113503
[21] Scime E E *et al* 2010 *Phys. Plasmas* **17** 055701
[22] Kline J L and Scime E E 2003 *Phys. Plasmas* **10** 1
[23] Palomares J M, Graef W A A D, Hübner S and van der Mullen J J A M 2013 *Spectrochim. Acta* B **88** 156
[24] Aramaki M, Ogiwara K, Etoh S, Yoshimura S and Tanaka M Y 2009 *Rev. Sci. Instrum.* **80** 053505
[25] Boffard J B, Piech G A, Gehrke M F, Anderson L W and Lin C C 1999 *Phys. Rev.* A **59** 2749
[26] Leonhardt D, Eddy C R, Shamamian V A, Fernsler R F and Butler J E 1998 *J. Appl. Phys.* **83** 2971
[27] Short Z D, Siddiqui M U, Henriquez M F, McKee J S and Scime E E 2016 *Rev. Sci. Instrum.* **87** 013505
[28] Keesee A M, Scime E E and Boivin R F 2004 *Rev. Sci. Instrum.* **75** 4091
[29] Keesee A M and Scime E E 2006 *Rev. Sci. Instrum.* **77** 10F304
[30] Keesee A M and Scime E E 2007 *Plasma Sources Sci. Technol.* **16** 742–49
[31] Greig A, Charles C and Boswell R W 2016 *Phys. Plasmas* **23** 013508
[32] Chu F, Mattingly S W, Berumen J, Hood R and Skiff F 2017 *J. Instrum.* **12** C11005
[33] Chu F and Skiff F 2018 *Phys. Plasmas* **25** 013506
[34] Katori H and Shimizu F 1993 *Phys. Rev. Lett.* **70** 3545
[35] Hübner S, Sadeghi N, Carbone E A D and van der Mullen J J A M 2013 *J. Appl. Phys.* **113** 143306
[36] Wiese W L, Brault J W, Danzmann K, Helbig V and Kock M 1989 *Phys. Rev.* A **39** 2461–71
[37] Boivin R F and Scime E E 2003 *Rev. Sci. Instrum.* **74** 4352
[38] Goeckner M J, Goree J and Sheridan T E 1993 *Rev. Sci. Instrum.* **64** 996
[39] Claire N, Bachet G, Stroth U and Doveil F 2006 *Phys. Plasmas* **13** 062103
[40] Scime E E, Keiter P A, Balkey M M, Kline J L, Sun X, Keesee A M, Hardin R A, Biloiu I A, Houshmandyar S and Chakraborty Thakur S 2015 *J. Appl. Phys.* **81** 345810103
[41] Thompson D S, Henriquez M F, Scime E E and Good T N 2017 *Rev. Sci. Instrum.* **88** 103506
[42] Hargus W, Lubkeman J, Remy K and Gonzales A 2012 Investigation of singly ionized iodine spectroscopy in support of electrostatic propulsion diagnostics development *48th AIAA/ASME/SAE/ASEE Joint Propulsion Conf. and Exhibit* (https://doi.org/)
[43] Fehsenfeld F, Evenson K and Broida H 1964 *Rev. Sci. Instrum.* **36** 294–8
[44] Severn G D, Edrich D A and McWilliams R 1998 *Rev. Sci. Instrum.* **69** 10
[45] Moore C E 1971 *Atomic Energy Levels* vol 1 (Washington, DC: Natl. Bur. Stds.) p 35
[46] Marr G V 1968 *Plasma Spectroscopy* (Amsterdam: Elsevier)